Focus Section: Data Mine: 2019 Ridgecrest, California, Earthquake Sequence

Waveform Cross-Correlation Relocation and Focal Mechanisms for the 2019 Ridgecrest Earthquake Sequence

Guoqing Lin*[1]

Abstract

I present a high-precision earthquake relocation catalog and first-motion focal mechanisms before and during the 2019 Ridgecrest earthquake sequence in eastern California. I obtain phase arrivals, first-motion polarities, and waveform data from the Southern California Earthquake Data Center for more than 24,000 earthquakes with the magnitudes varying between –0.7 and 7.1 from 1 January to 31 July 2019. I first relocate all the earthquakes using phase arrivals through a previously developed 3D seismic-velocity model and then improve relative location accuracies using differential times from waveform cross correlation. The majority of the relocated seismicity is distributed above 12 km depth. The seismicity migration along the northwest–southeast direction can be clearly seen with an aseismic zone near the Coso volcanic field. Focal mechanisms are solved for all the relocated events based on the first-motion polarity data with dominant strike-slip fault solutions. The M_w 6.4 and 7.1 earthquakes are positioned at 12.45 and 4.16 km depths after the 3D relocation, respectively, with strike-slip focal solutions. These results can help our understanding of the 2019 Ridgecrest earthquake sequence and can be used in other seismological and geophysical studies.

Cite this article as Lin, G. (2020). Waveform Cross-Correlation Relocation and Focal Mechanisms for the 2019 Ridgecrest Earthquake Sequence, *Seismol. Res. Lett.* **91**, 2055–2061, doi: 10.1785/0220190277.

Supplemental Material

Introduction

On 4 July 2019, a moment magnitude (M_w) 6.4 earthquake struck about 13 km southwest of Searles Valley, California. The majority of the aftershocks trend in the northeast–southwest direction, intersecting with the Little Lake fault zone (LLFZ) near Ridgecrest (Fig. 1). On the next day, about 9 km to the northwest, another earthquake of M_w 5.4 occurred, followed by a larger M_w 7.1 earthquake about 16 hr later. Since then, a great number of aftershocks of all the three big earthquakes were recorded, including two more events above magnitude 5 within 1 hr occurrence of the M_w 7.1 event. Most of the aftershocks are located on the eastern side of Sierra Nevada and north of the left-lateral strike-slip Garlock fault, migrating in the northwest–southeast direction along the LLFZ and the Airport Lake fault zone. The seismicity appears to cease in the fault zone to the south side of Owens Lake, and there is an aseismic zone near the Coso volcanic field. In this article, I present a high-precision earthquake relocation catalog using a 3D seismic-velocity model and waveform cross-correlation data, and first-motion focal mechanisms for earthquakes before and during the 2019 Ridgecrest sequence.

Data Set

I download the seismic data used in this study from the Southern California Earthquake Data Center (SCEDC, 2013). These data are reviewed by the Southern California Seismic Network analysts (Hutton *et al.*, 2006) and include event origin times, locations, magnitudes, phase arrivals, first-motion polarities, and waveforms for 24,545 earthquakes from 1 January to 31 July 2019 near the three large earthquakes and their aftershock sequence, bounded by latitudes from 35.46° to 36.3° and longitudes from −118.15° to −117.15° (Fig. 1). To show the characteristics of the earthquake sequence, I plot the daily seismicity rate and earthquake magnitude distribution during the time period of this study (Fig. 2). The magnitudes vary from −0.7 to 7.1, and more than 98% of them are local magnitudes. Data in August 2019 are also plotted for reference, but not processed for the results presented in this article.

Earthquake Relocation

Accurate earthquake locations together with high-quality velocity models are essential for seismic hazard assessments. They are necessary for determining accurate focal mechanisms, developing ground-motion models, and relating seismicity to

1. Department of Marine Geosciences, Rosenstiel School of Marine and Atmospheric Science, University of Miami, Miami, Florida, U.S.A.

*Corresponding author: glin@rsmas.miami.edu

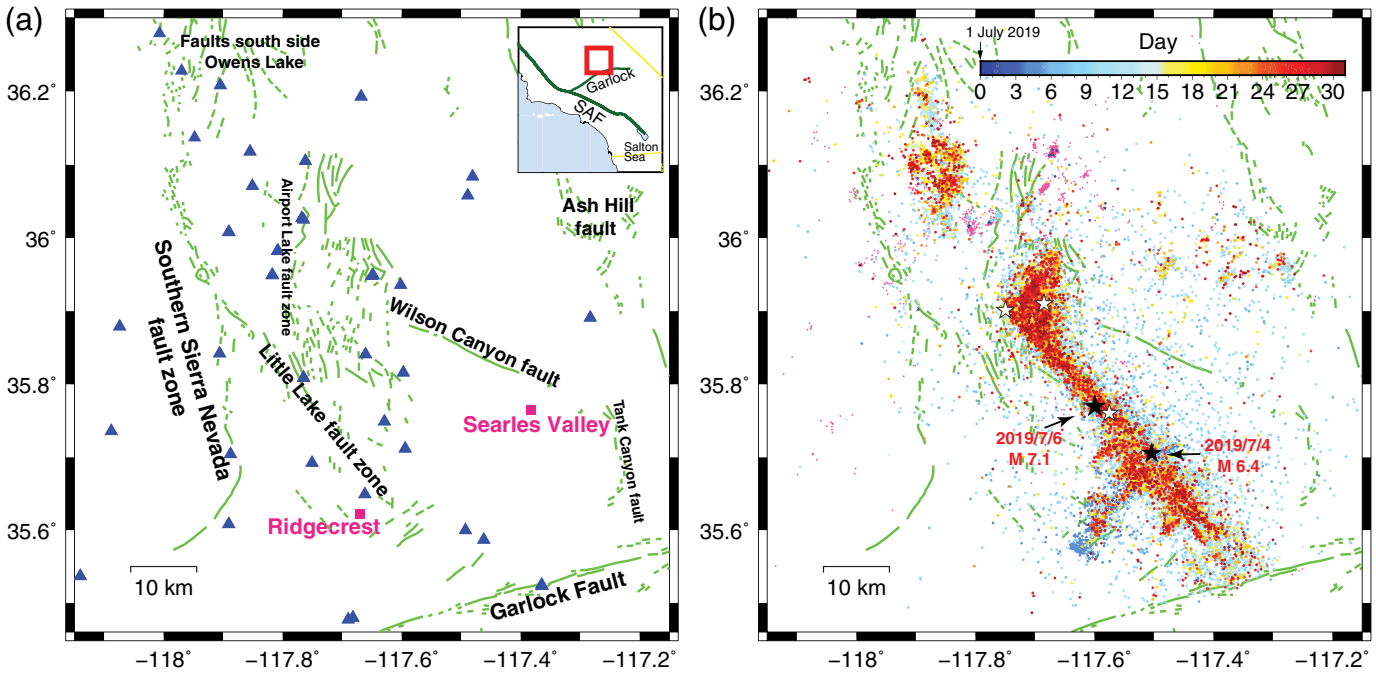

Figure 1. (a) Major geological features in the study area. Dark blue triangles stand for the seismic stations used in this study. Green lines represent major fault lines. Pink squares denote the city locations of Searles Valley and Ridgecrest. Red box in the inset map encloses the study area of this article in California (San Andreas fault [SAF]). (b) Southern California Earthquake Data Center (SCEDC) locations for earthquakes from January to July 2019 in the study area. Events are colored by days since 1 July 2019. Pink dots represent background seismicity before 1 July 2019. Stars mark events above magnitude 5 during the Ridgecrest sequence, including the M_w 6.4 and 7.1 earthquakes on 4 and 6 July 2019 (UTC), whose sizes are proportional to the corresponding event magnitude. The color version of this figure is available only in the electronic edition.

geologic structures (e.g., Hardebeck and Shearer, 2002; Kohler *et al.*, 2003). To improve absolute location accuracies, I apply the simul2000 tomographic algorithm (Thurber, 1983, 1993; Eberhart-Phillips, 1990) to relocate all the events with more than four first-arrivals using a recent 3D seismic-velocity model for the Coso geothermal field and the nearby region (Zhang and Lin, 2014), which covers the study area in this article (Fig. 1). A total of 423,087 *P* arrivals and 218,503 *S* arrivals were used in the inversion, during which both *P*- and *S*-velocity models were fixed, and only earthquake locations were perturbed for a few iterations until convergence. The absolute location errors are calculated for each event by the simul2000 algorithm. For all the 23,334 events relocated by the 3D model, the median of the absolute location uncertainties is 75 m for horizontal and 108 m for vertical.

Relative earthquake locations can be improved dramatically using the very precise differential times obtained from waveform cross correlation, which can often be measured to millisecond precision for similar events, allowing relative earthquake location precise to a few meters (e.g., Shearer, 2002; Hauksson and Shearer, 2005; Schaff and Waldhauser, 2005; Shearer *et al.*, 2005; Lin *et al.*, 2007, 2014; Hauksson *et al.*, 2012; Zhang and Lin, 2014). To further improve relative earthquake location accuracies, I calculate differential times from waveform cross correlation. The waveform data are first resampled to a uniform 100 Hz rate using a spline interpolation method. Because it has been found that the cross correlations are more reliable between 1 and 10 Hz (Shearer *et al.*, 2005; Lin *et al.*, 2007; Zhang and Lin, 2014), a band-pass filter is applied to the resampled data. I then perform waveform cross correlation for each event with up to 100 closest neighbors within 2 km distance and apply the differential-time relocation method to all the earthquakes using the XCORLOC location package (Lin, 2018). Correlation information is saved for more than 1 million event pairs with more than 164 million differential times. I then start the differential-time relocation from the 3D relocations. For each target event, only differential times with normalized correlation coefficients greater than 0.55 are used in the relocation process. Each event must have more than four differential times with correlation coefficients greater than 0.6. Relative location uncertainties are estimated by applying a bootstrap approach (Efron and Tibshirani, 1991), in which the differential times for each event are randomly resampled. I repeat this process 20 times for each event and relocate the event using the resampled differential times. The standard deviations of the 20 relocations are taken as the location errors for each event.

$M \geq 4$ earthquakes generally do not cross-correlate well with smaller events because of their more complicated waveforms and frequent clipping of their records. Bachura and Fischer (2019)

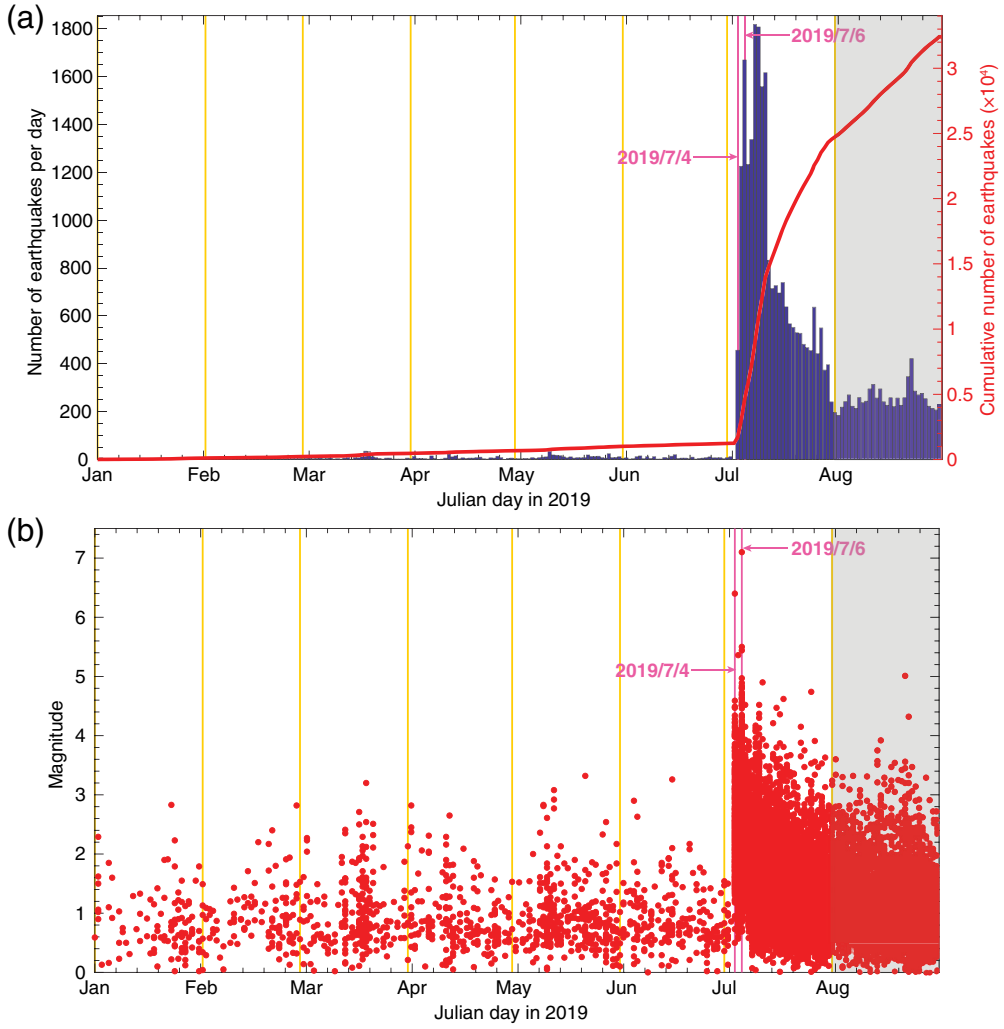

Figure 2. (a) Daily seismicity rate in the study area from 1 January to 31 July 2019. Red thick curve illustrates the cumulative number of earthquakes. (b) Magnitude distribution in the same time period. Pink vertical lines mark 4 and 6 July 2019 (UTC), when the M_w 6.4 and 7.1 earthquakes occurred. August 2019 data are plotted here for reference, but not processed in the results presented in this article. The color version of this figure is available only in the electronic edition.

showed that pulse width for earthquakes with large-magnitude difference is incomparable, which deteriorates the delay measurements and may result unreliable locations for large events. Therefore, I excluded the 101 local $M \geq 4$ events in the waveform cross-correlation relocation and used their 3D locations for focal mechanism calculation. For the final 21,819 relocated earthquakes (about 94% of the input events), the median of the relative location uncertainties is 8 m for horizontal and 16 m for vertical, respectively.

First-Motion Focal Mechanism

Assuming double-couple fault-plane solutions, I compute first-motion focal mechanisms for all the relocated events using the HASH program (Hardebeck and Shearer, 2002). Four different 1D velocity models, from previous earthquake location and tomography studies for southern California and the Coso area (Shearer *et al.*, 2005; Lin *et al.*, 2007; Zhang and Lin, 2014), are used to compute takeoff angles. Other input parameters for the inversion were selected in the same way as in Lin and Okubo (2016). I obtain focal solutions for 11,668 events based on more than 0.22 million *P*-wave first-motion polarity data measured on the vertical component of each seismic station. I use the same criteria for four types of qualities (A–D), as in Lin and Okubo (2016), based on the mechanism probability, the root mean square fault-plane uncertainty, the average misfit, and the station distribution ratio. In this article, I only present and discuss the 2395 mechanisms of quality A, B, and C, considered as good-quality solutions.

Results

In Figure 3, I show the location comparison of three catalogs: (1) the SCEDC location catalog; (2) the 3D relocation catalog; and (3) the final earthquake catalog that is relocated using both the 3D velocity model and waveform cross-correlation data. Only events in the final catalog are presented in these comparisons, that is, the same number of earthquakes are plotted. All depths in this article are relative to mean sea level, which is about 1 km below the ground surface. The main difference between the SCEDC and the 3D relocations are in absolute locations, especially for shallow events. The final relocation catalog shows much sharper features than the initial catalog (Fig. 3), similar to the template-matching catalog by Ross *et al.* (2019). A striking feature along profile C–D is the more than 15-kilometer-long aseismic zone near the Coso volcanic field, agreeing with the conclusion that the Coso geothermal field is not as sensitive to remote triggering as the adjacent fault zones by Zhang *et al.* (2017), although positive Coulomb stress changes were observed in the area from preliminary calculations (Rollins *et al.*, 2019; Toda and Stein, 2019). In Figure 4, I show similar

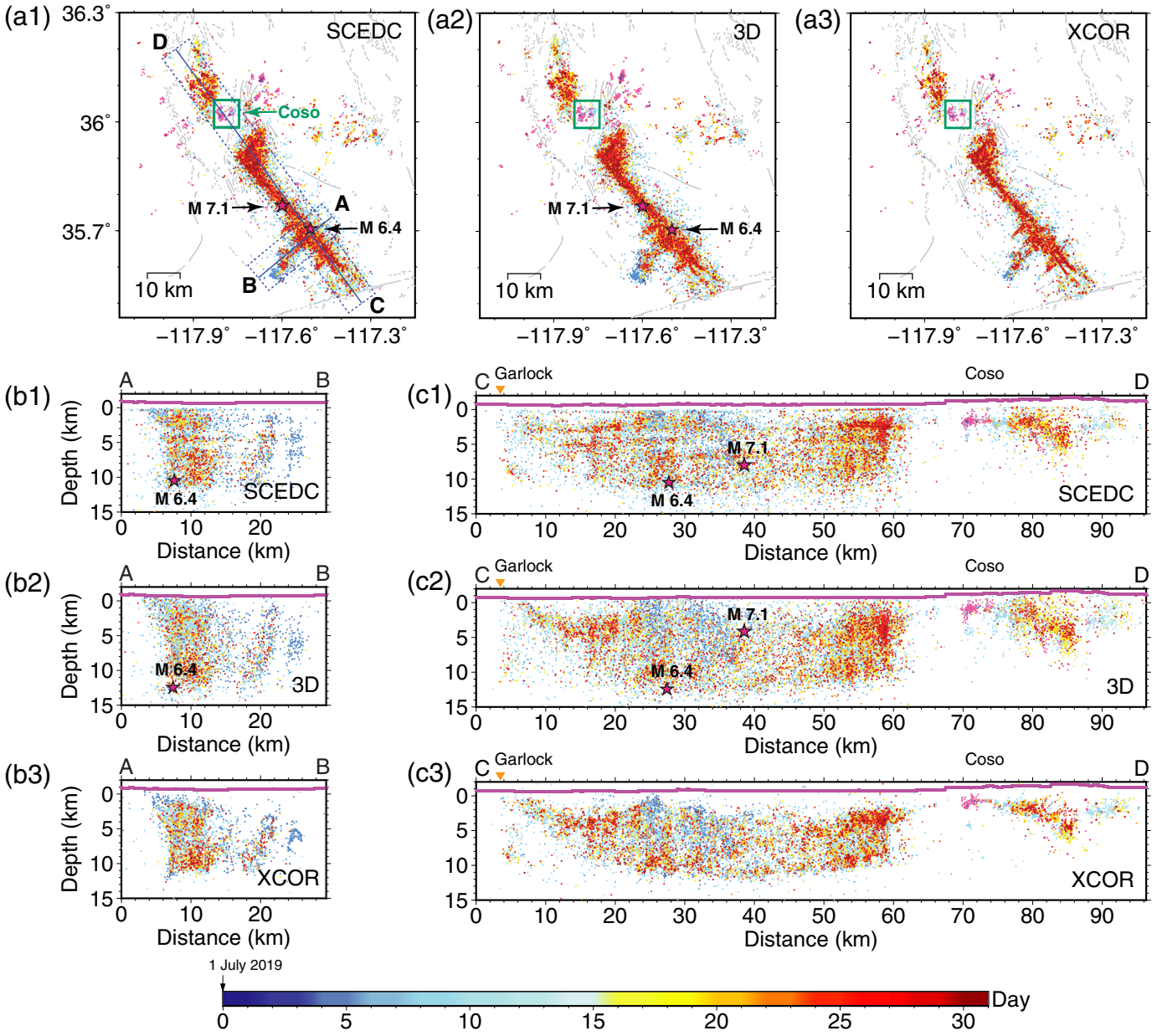

location comparison in Coso, defined by the geothermal well locations downloaded from the Division of Oil, Gas, and Geothermal Resources (orange triangles). The majority of the earthquakes during the 2019 sequence occurred in the northeast boundary and are relocated slightly deeper than the background-induced seismicity. The depth difference between the SCEDC and final relocation catalog is probably due to the different velocity models used in the location.

For the presentation purpose, I plot the resolved focal mechanisms in terms of their corresponding scalar focal type (Fig. 5). The scalar solutions, varying from −1 (normal) to 0 (strike slip) to 1 (reverse), are defined based on the rake angles of the two nodal planes and are classified using an x_f number between 0 and 1 (Shearer *et al.*, 2006; Lin and Okubo, 2016):

Figure 3. Location comparison for the 21,819 earthquakes from January to July 2019. (a1,b1,c1) SCEDC catalog; (a2,b2,c2) 3D relocation catalog; and (a3,b3,c3) waveform cross-correlation location catalog. Note that the same number of earthquakes are plotted in the three catalogs. Events are colored by days since 1 July 2019. Pink dots represent background seismicity before 1 July 2019. In (a1–a3). Gray lines denote major fault lines, and green boxes enclose the Coso volcanic field shown in Figure 4. Blue straight lines and dotted boxes in (a1) are the profiles and boundaries for the cross sections shown in (b1–b3) and (c1–c3). The purple curve at the top of each cross section illustrates local topography. Zero depth corresponds to mean sea level. The M_w 6.4 and 7.1 earthquakes are represented by stars in the SCEDC and 3D relocations. The color version of this figure is available only in the electronic edition.

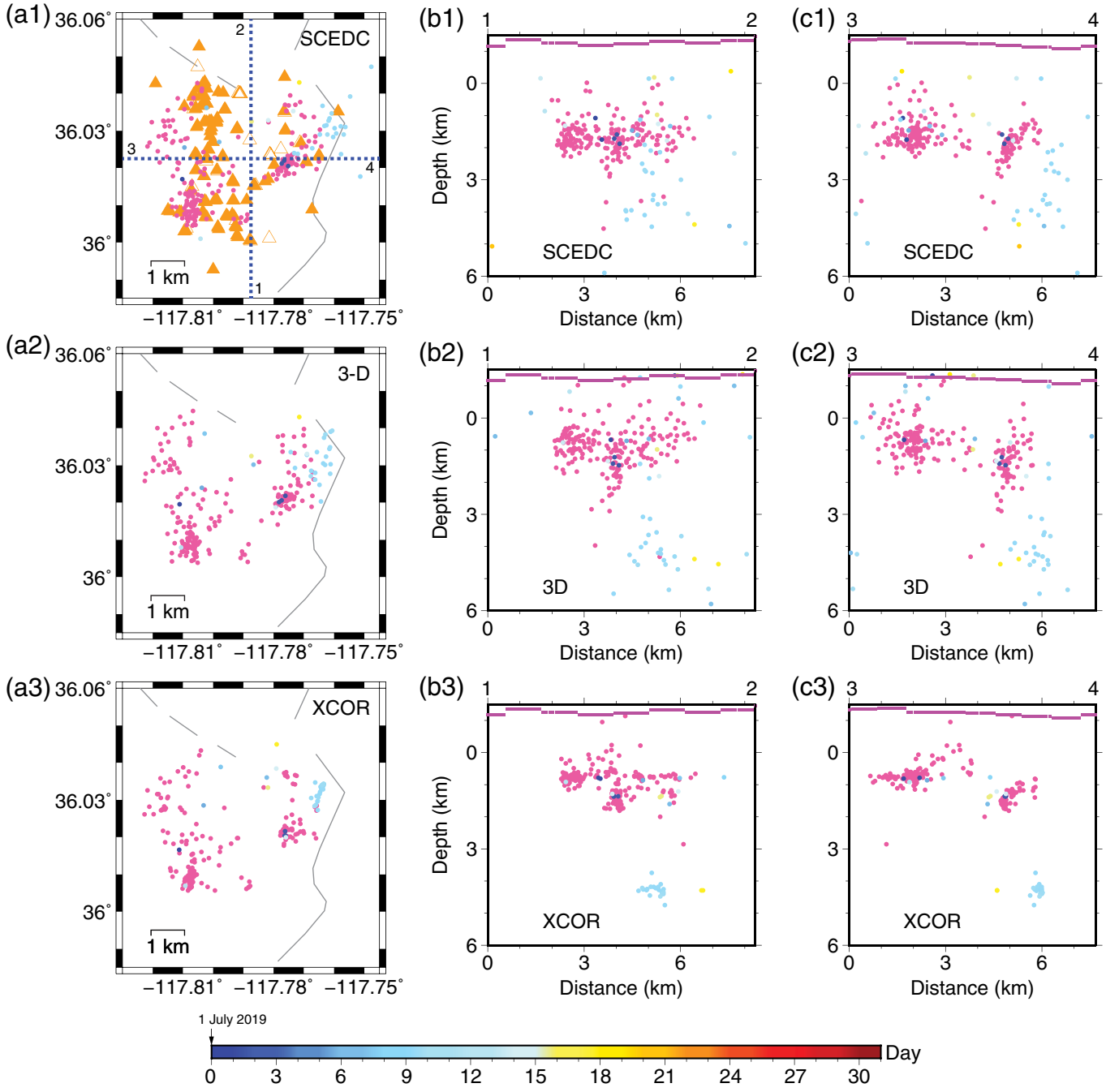

$$\begin{cases} -1 \le \text{scalar faulting} < -x_f, & \text{normal;} \\ -x_f \le \text{scalar faulting} \le x_f, & \text{strike-slip;} \\ x_f < \text{scalar faulting} \le 1, & \text{reverse.} \end{cases} \quad (1)$$

In this study, I select 0.33 for x_f to divide [−1, 1] into three equal segments. Both the focal mechanisms along the two profiles show dominant (~50%) strike-slip focal solutions, including the M_w 6.4 and 7.1 earthquakes.

Summary

The aftershock activity of the 2019 Ridgecrest earthquake sequence is continuing at the time of writing (September

Figure 4. Location comparison for 227 earthquakes in the Coso area. (a1,b1,c1) SCEDC catalog; (a2,b2,c2) 3D location catalog; and (a3,b3,c3) waveform cross-correlation location catalog. Note that the same number of earthquakes are plotted in the three catalogs. Events are colored by days since 1 July 2019. Pink dots represent background seismicity before 1 July 2019. In (a1), orange triangles represent the geothermal well locations (solid for active and open for abandoned) downloaded from the Division of Oil, Gas, and Geothermal Resources, and blue dotted lines are the profiles for the cross sections shown in (b1–b3) and (c1–c3). Gray lines in (a1–a3) denote major fault lines. The purple curve at the top of each cross section illustrates local topography. Zero depth corresponds to mean sea level. The color version of this figure is available only in the electronic edition.

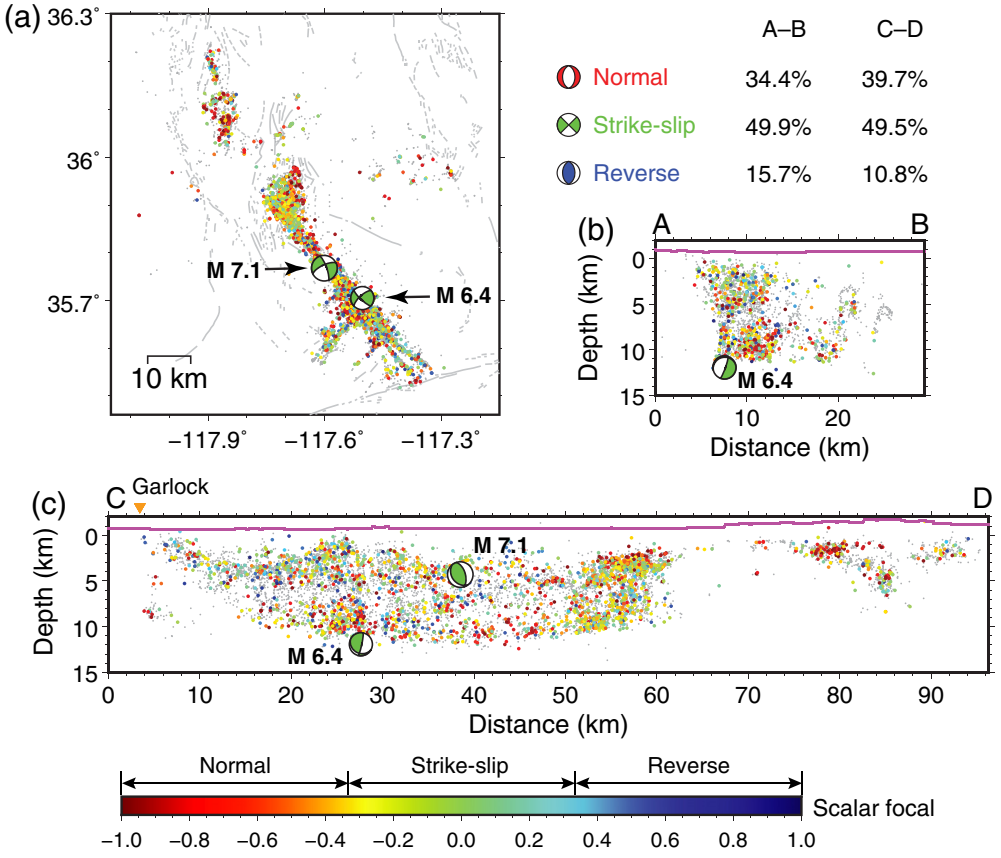

Figure 5. Distribution of the scalar focal solutions for the waveform cross-correlation relocated earthquakes. (a) Map view; (b,c) cross sections along profiles A–B and C–D shown in Figure 3(a1). Robust focal solutions are colored by the corresponding scalar focal type. Gray dots represent events with poorly resolved focal solutions. Focal mechanism plots are shown for the M_w 6.4 and 7.1 earthquakes at their 3D relocations in both map view and cross sections. Percentage of each focal type is shown for profiles A–B and C–D, respectively. Other symbols are the same as those in Figure 3. The color version of this figure is available only in the electronic edition.

2019) and may last for years. The purpose of this article is to provide a high-precision earthquake relocation catalog and first-motion focal mechanisms for events before and during the sequence. Both catalogs are available in the supplemental material and will be updated for more recent seismic activity on author's website (see Data and Resources). The map view and cross-sections of the relocation catalog, same as Figure 3 (a3,b3,c3), are also included in the supplemental material for user's reference (Figs. S1 and S2).

Data and Resources

Seismic data used in this study were accessed through the Southern California Earthquake Data Center (SCEDC) and published work. The fault and topography data were downloaded from the U.S. Geological Survey. Figures were made using the public domain Generic Mapping Tools (GMT) software (Wessel and Smith, 1991) and MATLAB (www.mathworks.com/products/matlab). Supplemental material includes the earthquake relocation catalog and first-motion focal mechanisms presented in this article and their format descriptions. Future releases of both catalogs will be available from the author's website at http://www.gqlin.com. All websites were last accessed in October 2019.

Acknowledgments

The author thanks the Southern California Earthquake Data Center (SCEDC) for maintaining the seismic networks and making the data available to this research. The author is grateful for the constructive and detailed reviews from Leonardo Seeber and two anonymous reviewers.

References

Bachura, M., and T. Fischer (2019). Waveform cross-correlation for differential time measurement: Bias and limitations, *Seismol. Res. Lett.* **90,** doi: 10.1785/0220190096.

Eberhart-Phillips, D (1990). Three-dimensional *P* and *S* velocity structure in the Coalinga region, California, *J. Geophys. Res.* **95,** 15,343–15,363.

Efron, B., and R. Tibshirani (1991). Statistical data analysis in the computer age, *Science* **253,** no. 5018, 390–395.

Hardebeck, J., and P. Shearer (2002). A new method for determining first-motion focal mechanisms, *Bull. Seismol. Soc. Am.* **92,** no. 6, 2264–2276.

Hauksson, E., and P. Shearer (2005). Southern California hypocenter relocation with waveform cross-correlation, part 1: Results using the double-difference method, *Bull. Seismol. Soc. Am.* **95,** no. 3, 896–903.

Hauksson, E., W. Yang, and P. M. Shearer (2012). Waveform relocated earthquake catalog for Southern California (1981 to June 2011), *Bull. Seismol. Soc. Am.* **102,** 2239–2244, doi: 10.1785/0120120010.

Hutton, K., E. Hauksson, J. Clinton, J. Franck, A. Guarino, N. Scheckel, D. Given, and A. Yong (2006). Southern California Seismic Network update, *Seismol. Res. Lett.* **77,** no. 3, 389–395, doi: 10.1785/gssrl.77.3.389.

Kohler, M., H. Magistrale, and R. Clayton (2003). Mantle heterogeneities and the SCEC reference three-dimensional seismic velocity model version 3, *Bull. Seismol. Soc. Am.* **93,** no. 2, 757–774.

Lin, G. (2018). The source-specific station term and waveform cross-correlation earthquake location package and its applictions

to California and New Zealand, *Seismol. Res. Lett.* **89,** no. 5, 1877–1885.

Lin, G., and P. G. Okubo (2016). A large refined catalog of earthquake relocations and focal mechanisms for the Island of Hawai'i and its seismotectonic implications, *J. Geophys. Res.* **121,** no. 7, doi: 10.1002/2016JB013042.

Lin, G., P. M. Shearer, and E. Hauksson (2007). Applying a three-dimensional velocity model, waveform cross correlation, and cluster analysis to locate Southern California seismicity from 1981 to 2005, *J. Geophys. Res.* **112,** no. B12309, doi: 10.1029/2007JB004986.

Lin, G., P. M. Shearer, R. S. Matoza, P. G. Okubo, and F. Amelung (2014). Three-dimensional seismic velocity structure of Mauna Loa and Kilauea volcanoes in Hawaii from local seismic tomography, *J. Geophys. Res.* **119,** no. 5, 4377–4392, doi: 10.1002/2013JB010820.

Rollins, C., R. S. Stein, G. Lin, and D. Kilb (2019). The Ridgecrest earthquakes: Torn ground, nested foreshocks, Garlock shocks, and Temblor's forecast, *Temblor*, doi: 10.32858/temblor.039.

Ross, Z. E., B. Idini, Z. Jia, O. L. Stephenson, M. Zhong, X. Wang, Z. Zhan, M. Simons, E. J. Fielding, S.-H. Yun, *et al.* (2019). Hierarchical interlocked orthogonal faulting in the 2019 Ridgecrest earthquake sequence, *Science* **366,** no. 6463, 346, doi: 10.1126/science.aaz0109.

Schaff, D. P., and F. Waldhauser (2005). Waveform cross-correlation-based differential travel-time measurements at the Northern California Seismic Network, *Bull. Seismol. Soc. Am.* **95,** no. 6, 2446–2461.

Shearer, P. M. (2002). Parallel fault strands at 9-km depth resolved on the Imperial fault, southern California, *Geophys. Res. Lett.* **29,** no. 14, doi: 10.1029/2002GL015302.

Shearer, P. M., E. Hauksson, and G. Lin (2005). Southern California hypocenter relocation with waveform cross-correlation, part 2: Results using source-specific station terms and cluster analysis, *Bull. Seismol. Soc. Am.* **95,** no. 3, 904–915.

Shearer, P. M., G. A. Prieto, and E. Hauksson (2006). Comprehensive analysis of earthquake source spectra in Southern California, *J. Geophys. Res.* **111,** no. B06, 303, doi: 10.1029/2005JB003979.

Southern California Earthquake Data Center (SCEDC) (2013). Southern California Earthquake Center, *Caltech. Dataset*, doi: 10.7909/C3WD3xH1.

Thurber, C. H. (1983). Earthquake locations and three-dimensional crustal structure in the Coyote Lake area, central California, *J. Geophys. Res.* **88,** no. B10, 8226–8236.

Thurber, C. H. (1993). Local earthquake tomography: Velocities and Vp/Vs-theory, in *Seismic Tomography: Theory and Practice*, H. M. Iyer and K. Hirahara (Editors), Chapman and Hall, London, United Kingdom, 563–583.

Toda, S., and R. Stein (2019). Ridgecrest earthquake shut down cross-fault aftershocks, *Temblor*, doi: 10.32858/temblor.043.

Wessel, P., and W. H. F. Smith (1991). Free software helps map and display data, *Eos Trans. AGU* **72,** 441.

Zhang, Q., and G. Lin (2014). Three-dimensional Vp and Vp/Vs models in the Coso geothermal area, California: Seismic characterization of the magmatic system, *J. Geophys. Res.* **119,** no. 6, 4907–4922, doi: 10.1002/2014JB010992.

Zhang, Q., G. Lin, Z. Zhan, X. Chen, Y. Qin, and S. Wdowinski (2017). Absence of remote earthquake triggering within the Coso and Salton Sea geothermal production fields, *Geophys. Res. Lett.* **44,** doi: 10.1002/2016GL071964.

Manuscript received 26 September 2019
Published online 26 February 2020